J Mater Sci: Mater Med (2008) 19:2781–2790
DOI 10.1007/s10856-007-3346-5

# Porous ceramic bone scaffolds for vascularized bone tissue regeneration

**Julia Will · Reinhold Melcher · Cornelia Treul · Nahum Travitzky · Ulrich Kneser · Elias Polykandriotis · Raymund Horch · Peter Greil**

Received: 6 August 2007 / Accepted: 5 December 2007 / Published online: 29 February 2008


**Abstract** Hydroxyapatite scaffolds with a multi modal porosity designed for use in tissue engineering of vascularized bone graft substitutes were prepared by three dimensional printing. Depending on the ratio of coarse (mean particle size 50 μm) to fine powder (mean particle size 4 μm) in the powder granulate and the sintering temperature total porosity was varied from 30% to 64%. While macroscopic pore channels with a diameter of 1 mm were created by CAD design, porosity structure in the sintered solid phase was governed by the granulate structure of the printing powder. Scaffolds sintered at 1,250 °C were characterized by a bimodal pore structure with intragranular pores of 0.3–0.4 μm and intergranular pores of 20 μm whereas scaffolds sintered at 1,400 °C exhibit a monomodal porosity with a maximum of pore size distribution at 10–20 μm. For in-vivo testing, matrices were implanted subcutaneously in four male Lewis rats. Scaffolds with 50% porosity and an average pore size of ~18 μm were successfully transferred to rats and vascularized within 4 weeks.

J. Will (✉) · R. Melcher · C. Treul · N. Travitzky · P. Greil
Department of Materials Science (Glass and Ceramics), University of Erlangen-Nürnberg, Martensstr. 5, 91058 Erlangen, Germany
e-mail: Julia.will@ww.uni.-erlangen.de

U. Kneser · E. Polykandriotis · R. Horch
Department of Plastic and Hand Surgery, Medical Center, University of Erlangen-Nürnberg, Krankenhausstraße 12, 91054 Erlangen, Germany

## 1 Introduction

Bone grafting to replace missing bone with synthetic porous material (bone graft scaffolds) able to encourage new bone ingrowth and remodelling of bone have been investigated for over 30 years [1]. Over 2 million bone graft procedures are performed annually world-wide. Ninety percent of these procedures used natural bone from autografts or allografts, while only 10% used synthetic materials [2]. Limited availability of autografts and the risk of disease transfer of allografts, however, produce an increasing demand for synthetic bone grafts. Novel approaches for stimulating and accelerating of osteointegration, osteoconduction and osteoinduction of bioartificial bone substitutes focus on angiogenesis and vascularization by design of bioactive ceramic materials with appropriate porosity architecture [1]. There is a general consensus that a scaffold suitable for intrinsic vascularization must have a high porosity (>40–60%), and an interconnected pore structure providing a high permeability for fluid transport [3–5]. Effective pore diameters larger than 100 μm were reported to be adequate to induce osteoconductivity [6–8].

The turning point of any given scaffold towards biointegration and tissue specific function is its transition from an inert structural backbone to a vascularized construct interacting with its vivo environment. In the classic models of neovascularization, the matrices were subjected to fibrovascular invasion from the surrounding tissues, depending on the site of implantation. Intraabdominal, subcutaneous and intramuscular implantation has been reported [9–11]. This mode of neovascularization was termed "extrinsic" vascularization since the new capillaries grew into the matrix as a result of local inflammation around the implant [12]. However, this method included a plethora of limitations. An adequate neovascularization

precluded excellent local conditions in terms of perfusion and regenerating potential. Furthermore, in the experimental setting of cell loaded matrices, a slowly propagating angiogenesis with highly inflammatory components failed to sustain life and function of the co-transplanted cell populations [13]. The term "intrinsic" vascularization was coined for a novel approach encompassing a combination of a bioactive matrix with a vessel driving angiogenesis by means of vascular induction from the core of the matrix towards the periphery [14, 15]. Evolution of an adequate microvascular system is in this context highly independent from local conditions. Furthermore, the pattern of vascularity resembles that of an organoid amenable to microsurgical transplantation. Autologous tissue units of this form are used routinely in reconstructive surgery nowadays [16, 17].

Synthetic calcium phosphate ceramic based on hydroxyapatite $Ca_5(PO_4)_3OH$ (HA) is bioactive in the sense that it is a non-toxic compound and interfacial bonds are able to develop between HA and the living tissues leading to enhanced mechanical strength of the overall structure. While HA has excellent bioactivity, its poor mechanical properties compared with bone have hindered its clinical application. Strength of HA was found to show a strong correlation with sintering temperature, grain growth and porosity in the sintered bodies. Dense HA has a compressive strength (430–920 MPa) four times that of cortical bone (100–230 MPa), and yet a significantly lower tensile strength (17–110 MPa compared to 50–150 MPa of cortical bone) and fracture toughness (1 $MPam^{1/2}$ to 2–12 $MPam^{1/2}$) [2]. Significant enhancements in strength and fracture toughness of HA reportedly have been achieved by making composite materials, using various types of second phases, such as polymers, metals, ceramics, and carbon nanotubes as reinforcing agents [18–24]. Furthermore, HA has the advantage of abundant supply, low cost and absence of immunogenicity [25]. In particular, porous HA implants have served as bone substitute in the clinics for long time including replacement of bony and periodontal defects, alveolar ridge, augmentation of spine fusion, and ear/eye implantation [7, 8, 26–28]. Porosity in HA implants is used to reduce weight and to rapidly deliver calcium to support histological processes resulting in enhanced tissue growth and their binding with the scaffold surface [29]. Porous HA implants were produced by a variety of chemical processing methods including powder slurries which contain porogenic volatiles [30], impregnation and foaming of gels [31, 32] or hydrothermal conversion of biogenic coral skeleton carbonate [33]. All methods mentioned above, however, suffer from limited ability of controlling the size, shape, and interconnectivity of the pores resulting in low mechanical strength and low reproducibility of the sintered HA implant structures. For example, compressive strength of HA was found to be reduced to 30 MPa at a porosity of 50% [34]. Thus, precise control over porosity, pore size, and pore geometry is essential for the rational design of ceramic scaffolds with superior bone forming capability [8].

Three dimensional printing offers a novel approach not only to generate complex outer shape of implants but to create macro pore structures according to CAD or CT imaging data. Layerwise injection of a liquid binder into a powder bed of typical thickness between 50 and 200 μm finally builds up a three dimensional body which after removing unbonded powder can be post-processed into a porous implant structure [35]. Pre-processing of granulated powder with suitable flowing, packing and wetting behaviour is essential to achieve a high geometrical resolution required for controlled pore structure formation. Spray dried granulates were used for three dimensional printing of a variety of HA implants including those of low residual porosity as well as macroporous bodies [5, 36, 37]. HA constructs with pore channels having diameters of 500–1,000 μm were fabricated which were applied in osteoblast cell seeding investigations [38].

It was the aim of our work to use three dimensional printing for creation of HA implant bodies with an outer shape and an internal pore structure suitable for intrinsic vascularisation experiments. Starting from a bimodal mixture of large and small size HA powders the porosity, the sintering behaviour and the mechanical properties changed according to the different packing structure in the powder bed. The cylindrical HA implant constructs contained macroscopic pore channels and an equatorial groove for fixing the arteria/vena loop prepared by microsurgery. In vivo vascularization behaviour was tested in a rat model and confirmed the high vascularization potential of the printed HA implant design.

## 2 Experimental procedure

### 2.1 Powder processing

Two different hydroxyapatite (HA) powders with an average grain size of 50 μm (coarse) (Ceram GmbH, Albbruck-Birndorf, Germany) and of 4 μm (fine) (Merck, Darmstadt, Germany) were applied. The particle size distribution was measured by laser-granulometric analysis of the powder suspended in isopropanol (Master Sizer 2000/Hydro 2000S, Malvern Instruments, Malvern, GB) and the specific surface area by BET method using $N_2$ adsorption (ASAP 2000, Micromeretics, Mönchengladbach, Germany). The coarse powder consists of spray dried granules with a significantly smaller crystallite size of approximately 26 nm as derived from the specific surface area of 71.8 $m^2/g$ (specific surface

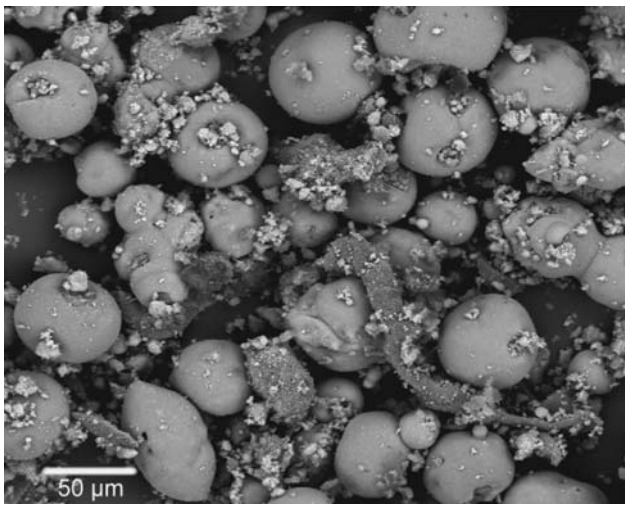


**Fig. 1** Microstructure of the milled powder mixture used for printing (C/F-60/40 + 15 wt.% binder (starch))

area $S_V = 6/(D \times \rho)$ with $D$ the mean particle diameter and $\rho$ the density (3.2 g/cm$^3$)). Calcination at 920 °C for 1 h in air resulted in a reduction of the specific surface to 8.5 m$^2$/g which corresponds to a mean particle size of 0.23 µm. Six different powder compositions were prepared with the weight ratio of coarse (C) to fine (F) powder (C/F ratio) varying from 85/15, 75/25, 60/40, 40/60, 25/75, to 0/100, respectively. Each of the six powder mixtures was thoroughly admixed with 15 wt.% (relating to the total quantity of HA powder) of a polysaccharide based binding agent (cellulose and starch) (ZP 14, Z-Corporation, Burlington, MA, USA). As an example Fig. 1 shows the microstructure of the milled powder mixture of C/F-60/40.

## 2.2 Printing and sintering

Computer aided design was applied to generate the macroscopic shape of the cylindrical implant bodies according to the clinical requirements for microsurcigal procedure. The diameter of the printed cylinder was 9 mm and the height 7 mm. A semicircular groove with a radius of 1.25 mm was set at the equator line in order to facilitate fixation of the axial arteria/vena vascularization loop by microsurgical preparation. Macroscopic pore channels with a diameter of 1 mm in the printed body were oriented parallel to the cylindrical axis to facilitate cell injection after pre-vascularisation. Indirect three dimensional printing (Z-Printer 310, Z-Corporation, Burlington, MA, USA) was performed by injection of the binder liquid into each individual powder layer. Table 1 shows the composition of the water based binder. The bubble jet print head (HP 10 black, Hewlett-Packard Inkjet Supplies, Amstelveen, NL) provides 304 nozzles in two rows with a nozzle diameter of 60 µm. The thickness of each individual powder bed layer was set to minimum 50 µm and the binder saturation was 0.7 g/cm$^3$. Since dilatometric measurements (Dil 402C, Netzsch, Selb, Germany) revealed a linear shrinkage of approximately 25% to take place upon sintering at 1,400 °C the sliced geometrical data of the implant dimensions were isotropically expanded by a factor of 1.25. The printed parts were dried within the powder bed for 24 h at room temperature. Binder burn out and sintering was carried out in an electrically heated furnace in air atmosphere. A slow heating rate of 1 °C/min was applied from room temperature to 600 °C to avoid fracture during binder burn out followed by a faster heating rate of 3 °C/min from 600 °C to the sintering temperature of 1,250 or 1,400 °C. After a dwell period of 1 h the specimens were cooled down to room temperature with a rate of 10 °C/min.

## 2.3 Microstructure characterization and mechanical properties

The sintered samples were embedded in epoxy-resin and polished to a 6 µm diamond finish, sputtered with gold and analysed by scanning electron microscopy (Quanta 200, FEI, Prague, Czech Republic). Cylindrical pore channel diameters were measured by optical microscopy (Leica M420, Leica, Heerbrugg, Switzerland). The open porosity was measured by means of Hg-porosimetry (Pascal 140, Thermo Electron, Rodano/Milan, Italy). Total porosity was derived from the geometrical density e.g. apparent density of the body which was determined by measuring the weight

**Table 1** Composition of binding liquid

| Content (wt.%) | | | Supplier |
|---|---|---|---|
| 94.5 | Water | 2× Distilled | – |
| 2.5 | Glycerin | Anhydrous, p.a. | Merck, Darmstadt, Germany |
| 1.0 | Polyethylene glycol | PEG 300 | Sigma-Aldrich, Steinheim, Germany |
| 1.0 | Fatty alcohol polyalkylene glycol ether | Propetal 160 | Zschimmer & Schwarz, Lahnstein/Ruhr, Germany |
| 0.5 | Polyvinyl alcohol | Mowiol 4-88 | Kuraray Specialties Europe, Frankfurt/Main, Germany |
| 0.5 | Potassium sorbate | p.a. | Fluka Chemie, Buchs, Switzerland |

and volume of the specimen body and the density of HA of 3.2 g/cm$^3$. X-ray diffraction profiles of the powders were recorded by powder diffractometry (Kristalloflex, D 500, Siemens, Karlsruhe, Germany) using monochromatic Cu-K$\alpha$ radiation with a scan rate of 1°/min over a 2$\Theta$ range of 20–45°.

The compressive strength was measured using universal testing machine (Instron 4204, Instron Corp., Canton/MA, USA) at a strain rate of 0.01 mm/s. For the strength measurements cylindrical samples of same length and diameter but without the macro pore channels and without the equatorial groove were prepared with the same conditions as used for the implant specimens. The samples were placed between two buffer gum layers to ensure uniformity of surface loading. The failure load was taken as the peak load. Mean fracture stresses were calculated from the cross-sectional areas and the failure loads of identical samples taking at least a minimum of ten samples.

### 2.4 In vivo vascularisation experiments

The printed and sterilized (vapour, 120 °C, 1.5 h) scaffolds were transferred to four syngenic male Lewis rats used as recipients. All implantation procedures took place under general anaesthesia with Isoflurane (Baxter, Unterschleißheim, Germany). Two of the hydroxyapatite bodies (CF-85/15 and CF-75/25, both sintered at 1,400 °C) were inserted into two subcutaneous pouches in the back of the animal. The surgical incision was placed laterally to the matrix and the pouch was formed by blunt dissection towards the median line. All animals received 0.2 mL Benzylpenicillin-Benzathin (Tardomycel, Bayer, Leverkusen, Germany), buprenorphin (0.3 mg/kg rat weight) (Temgesic, Essex Chemie AG, Luzern, Switzerland) and Heparine (80 IU/kg) (Liquemin, Ratiopharm, Germany) postoperatively. The matrices were left in situ for four weeks and were explanted after sacrifice of the animal with a $CO_2$ over-dose. All tissues were explanted in-toto in a standardized fashion and were fixed with 3.5% neutral buffered formalin. After fixation, the tissues were decalcified using EDTA solution, embedded in paraffin and 5 µm thick histological sections were prepared by standard methods and stained with haematoxylin and eosin (HE). Microphotographs were taken using a Leica microscope and digital camera. For further identification of a functional endothelium, immunohistochemistry with staining of endothelial cells for CD31 was used. Rat endothelial cells were detected immunohistochemically using the lectin Bandeiraea simplicifolia agglutinin. Paraffinated sections were treated in a xylol/ethanol sequence, and after rinsing in PBS solution, endogenous peroxidase activity was blocked in 30% hydrogen peroxide for 10 min. Blocking was completed with avidin and biotin 15 min each (Vector Laboratories, Burlingame, CA) as well as 5% normal goat serum for 1 h. Biotinylated lectin (Bandeiraea simplicifolia, Sigma) was applied 1:100 overnight at 48C. Solutions were diluted in PBS. Between incubation steps, slides were rinsed in PBS solution. For detection, Streptavidin AB Complex/horseradish peroxide (Dako GmbH, Hamburg, Germany), was applied for 30 min, followed by development with DABþChromogen (Dako GmbH). Sections from heart muscle served as positive controls and omission of the lectin as negative control.

## 3 Results and discussion

### 3.1 Powder composition and printing

Figure 2 shows the CAD model and the printed and sintered bone graft substitute (CF-75/25). Three dimensional printing involves *layer-by-layer* construction of the scaffold. The HA-starch powder mixture forming each layer was bonded by computer controlled local injection of binder liquid giving rise for partial cross-linking of starch. Since powder packing in the bonded powder segment will strongly influence not only the sintering behaviour and pore structure formation but also the mechanical properties of the porous scaffold bimodal mixtures of various coarse/fine powder ratio examined. The effect of the size distributions on packing characteristics of the particle have been primarily studied through physical experiments [39, 40] and through computer simulations [41, 42]. While the large particles (coarse) with a sphere like morphology provide excellent flow behaviour, the small particles (fine) are intended to increase the packing density by filling the interstitial space between the large particles and should promote sintering.

Figure 3 shows the variation of porosity in the printed and the sintered specimens as a function of the coarse/fine powder ratio in the printing powder. As to be expected from the principles of interstitial space filling addition of fine powder to the coarse powder results in a reduction of porosity ($V_p$) from 65% down to a minimum of 55% at a coarse/fine ratio of approximately 40/60. The expected porosity within the printed compact was calculated from the measured particle size distributions (not shown) of the coarse and fine HA powders according to the fractal-like concept of Andersson [43] modified by Funk and Dinger [44]

$$\frac{CPFT}{100} = \frac{D^n - D_S^n}{D_L^n - D_S^n} \quad (1)$$

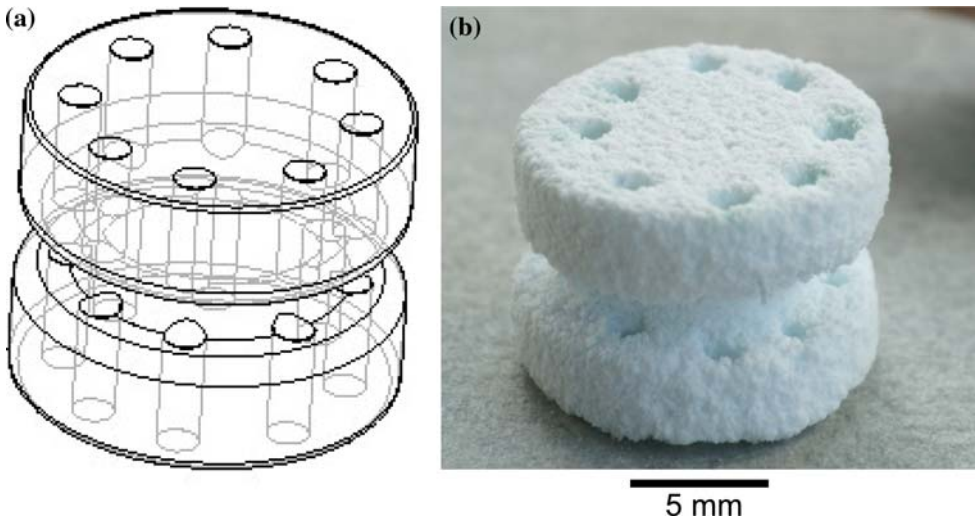


**Fig. 2** Bone regeneration construct for vascularization investigations: (**a**) CAD-model, (**b**) printed and sintered (CF-75/25)

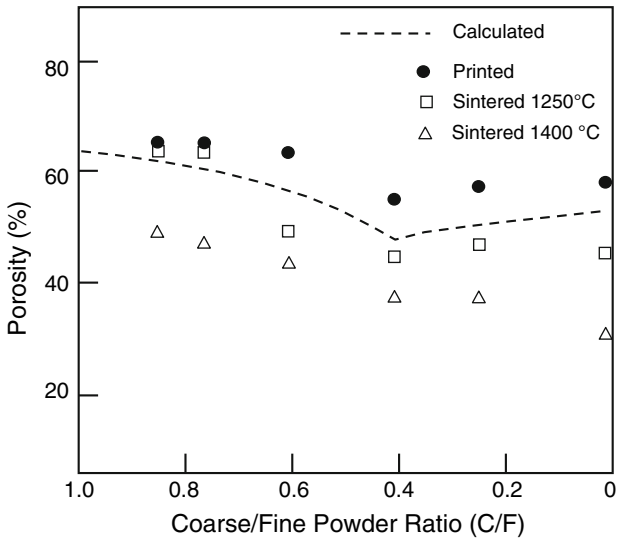


**Fig. 3** Porosity of the printed and sintered bone graft scaffolds as a function of coarse/fine powder ratio. Data points were measured by Hg-intrusion porosimetry. Porosity of the printed scaffold (no macroporosity) is compared to calculated porosity from Eq. 1

where *CPFT* is the cumulative percent finer than *D*, *D* is the measured particle size, $D_L$ is the largest particle diameter or size modulus, $D_S$ is the smallest particle diameter, and *n* is the distribution modulus. The total porosity, *Vp*, is obtained from the cumulative volume fraction finer than *D* (*CVFFT*) ($Vp = CVFFT$ at $D_S$ (100)) [45]. The calculated line confirms the trend as the measured data points of the printed samples with a distinct minimum of porosity at similar C/F = 40/60. Since the calculation is based on ideal packing of particles assuming an exponent of $n = 0.37$ for maximum packing efficiency, the shift observed between the measured and the calculated curves indicates a lower packing efficiency. In the case of flowing transport of the dry powder to sequentially built up individual layers of limited thickness (e.g. 50–100 μm) on the printing powder bed a low packing structure may be expected due to lack of rearrangement of irregularly shaped (non-spherical) coarse particles in unfavourable positions as well as fine particles bound to coarse grains by surface adhesion.

### 3.2 Sintering and microstructure

Shrinkage associated with sintering started at 800–1,000 °C and was finished at approximately 1,400 °C. Maximum of shrinkage rate was found at 1,250 °C and the total linear shrinkage of all powder mixtures attained 27% after sintering at 1,400 °C. While HA remained stable after sintering at 1,250 °C decomposition started above 1,300 °C [46]

$$Ca_{10}(PO_4)_6(OH)_2\ (HA) \rightarrow 2Ca_3(PO_4)_2\ (TCP) + Ca_4O(PO_4)_2\ (TeCP) + H_2O$$

as confirmed by XRD analysis showing small fractions (<10 wt.%) of (TeCP) (JCPDS 025-1137) and α-TCP (JCPDS 9-348) [8, 47] in the samples sintered at 1,400 °C. Figure 4 shows the sintered microstructures of the two powder mixtures C/F-75/25 and C/F-25/75. While the initial granulate structure remains almost unaffected in the material with the high fraction of coarse powder, densification in the powder mixtures containing a high fraction of fine particles resulted in loss of granular microstructure.

Initial porosity in the printed bodies decreased upon sintering by 15% (1,250 °C) to 35% (1,400 °C) with the densification being promoted with increasing fraction of fine HA powder. A minimum residual porosity of approximately 30% e.g. a fractional density of 0.7 was observed in the specimen sintered at 1,400 °C composed of fine powder fraction only. Porosity can be in the form of

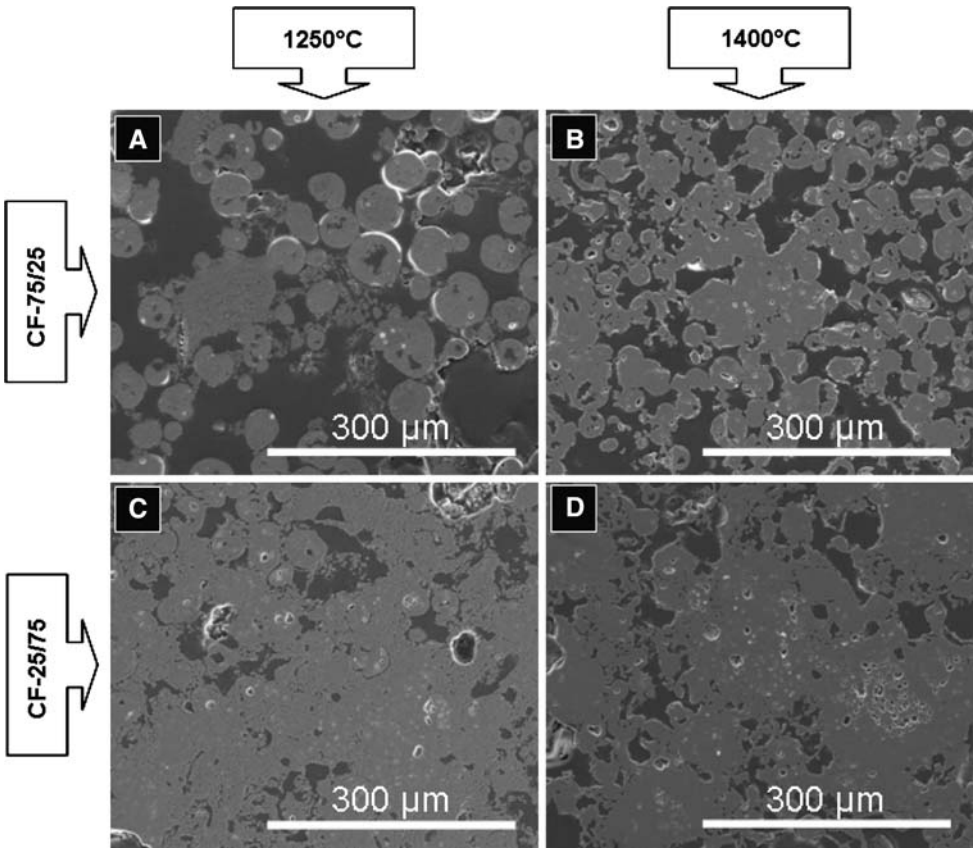


**Fig. 4** SEM-micrographs of samples processed from powder mixtures CF-75/25 and CF-25/75 sintered at 1,250 and 1,400 °C, respectively

micropores (<1 µm in diameter, due to incomplete sintering), mesopores (1–100 µm in diameter, formed by inter agglomerate pores) or macropores (>100 µm in diameter, created to permit invasion of endothelial system). Figure 5 shows typical pore size distributions obtained from the C/F-75/25 sample (cylindrical specimen without macropore channels). While the sample sintered at 1,250 °C still contained a submicron pore fraction with a peak maximum at 0.3 µm, the sample sintered at 1,400 °C only shows the pronounced pore size maximum at 15–20 µm.

### 3.3 Compression strength

Though adaptive bone formation process gives rise for a similar long term (>24 weeks) mechanical behaviour of porous bone graft scaffolds that had different compression strength before implantation [1], rapid vascularisation and assimilation were shown to be favoured by a high interconnected porosity in the scaffold. Increasing the total porosity volume, however, strongly deteriorates mechanical stability of the porous bone graft scaffold [48]. Figure 6 shows the relationship between composition and compression strength for samples sintered at 1,250 and 1,400 °C, respectively. A compressive strength of 31 ± 6 MPa was measured for cylindrical samples with the highest content of fine, ungrained particles, sintered at 1,400 °C. Slightly lower compressive strength ranging from 5 to 20 MPa was reported for printed HA with a porosity of 50% and pore sizes of 10–30 µm [49]. Based on the minimum solid area model [50] an exponential relation between the strength, $\sigma_c$, and the porosity, $V_P$, was derived to characterize the strength reduction with increasing porosity:

$$\sigma_c = \sigma_0 \exp(-bV_P) \quad (2)$$

$\sigma_0$ is zero-porosity strength ($V_P = 0$), and b is a coefficient related to the pore shape and pore orientation usually in the range of 2–7 [51]. Figure 7 shows that the compression strength data obtained from the printed HA samples are significantly lower compared to the calculated curve (2) taking the data reported from de Groot et al [52] of $\sigma_0 = 700$ MPa and $b = 5$. A similar relation was derived for the tensile strength, $\sigma_t$, with $\sigma_0 = 200$ MPa and $b = 20$ as a function of the volume fraction of microporosity $V_m$ (pores <1 µm in diameter, due to incomplete sintering) represented by curve (3). Since Eq. 2 is valid only for porosities <45% [50] a variety of relations for relating the strength with porosities >45% where no more the minimum contact area of solid particles but the growing area of pore windows is supposed to dominate the strength were derived. An extension of equ. (2) proposed by Tonyan

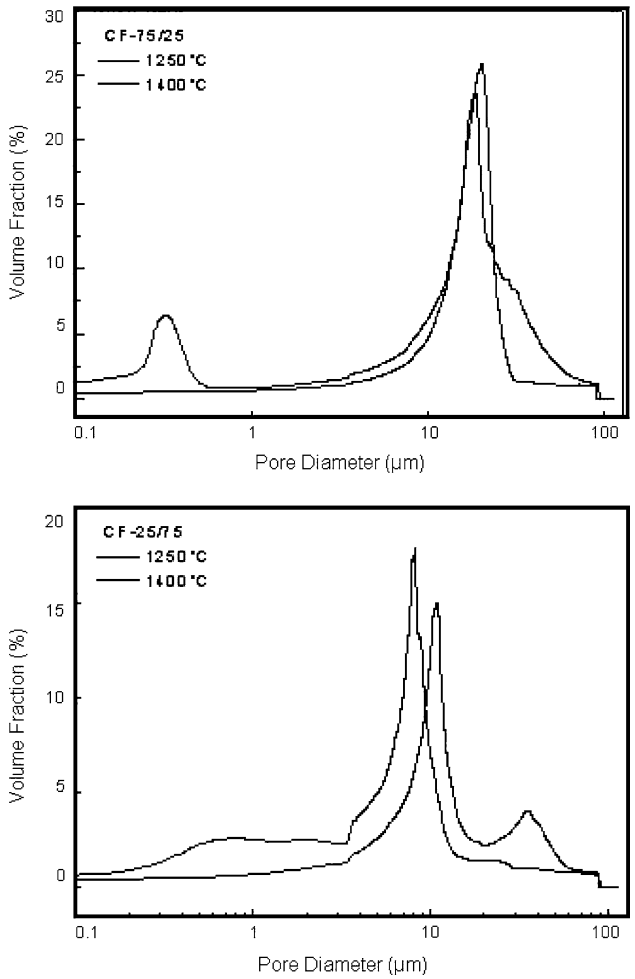


**Fig. 5** Pore size distributions (Hg-intrusion porosimetry) of sample C/F-75/25 sintered at 1,250 and 1,400 °C

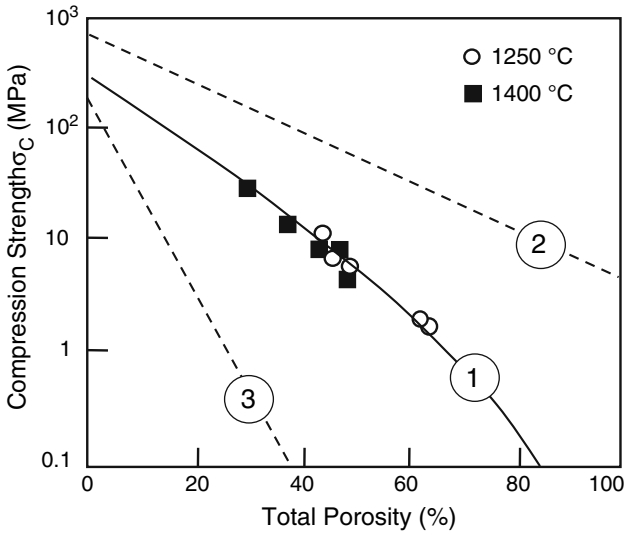


**Fig. 7** Porosity-strength correlation for samples sintered at 1,250 and 1,400 °C, respectively. Curves 2 and 3 were calculated according to Eq. 2 using data of [52] for compression (2) and tensile strength (3). Curve (1) was calculated from Eq. 3

and Gibson [53] takes into account various hierarchies of porosity based on a combination of minimum solid area model and open cellular foam mechanics (failure due to bending of cell struts) [54].

$$\sigma_c = \sigma_0 C\left(1 - V_p\right)^m \exp\left(-bV_p\right) \tag{3}$$

As may be recognized curve (1) in Fig. 7 calculated according to Eq. 3 with $C = 0.65$, $m = 2$, b = 5 and $\sigma_0 = 450$ MPa fits well to the experimental data for the specimens sintered at 1,400 °C characterized by

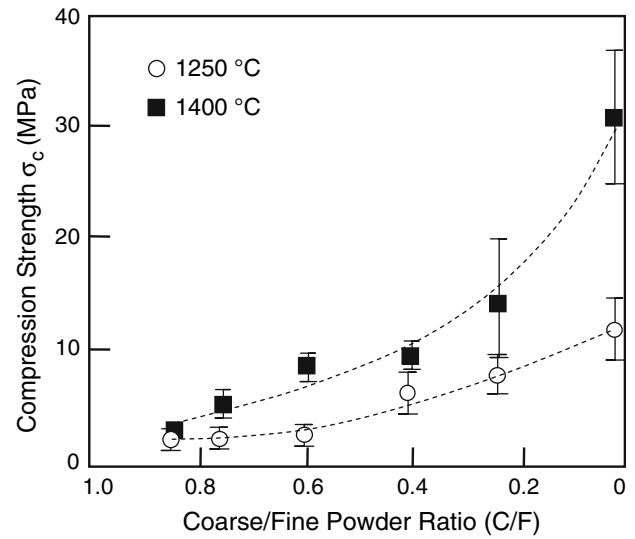


**Fig. 6** Compression strength of samples prepared from different C/F powder ratios sintered at 1,250 and 1,400 °C

**Fig. 8** In vivo experiments. Four weeks after subcutaneous implantation of a CF-85/15 scaffold scintered in 1,400 °C. The matrix is surrounded by a dense fibrous capsule. There are no signs of an abscess or skin perforation. The matrix is explanted in toto with surrounding tissue for further histological evaluation. The Canals for secondary application of cells or growth factors were incorporated in the design, here visible along the periphery of the bidiscal matrix

monomodal porosity as well as those with bimodal porosities sintered at 1,250 °C. For brittle foams ($V_p > 70\%$) the compression strength was reported to scale with $m = 3/2$ when cell crushing dominates whereas $m = 2$ when the foam fails by elastic buckling [54]. Though, microporosity in the solid strut sintered scaffold might give rise for the lower level of $\sigma_0$ compared to literature data of sintered and hot pressed HA materials [52], a lower strut stiffness was postulated to facilitate load distribution and may help to avoid unfavourable stress shielding effects [55]. Additionally it was demonstrated that a reduction of strut modulus associated with increasing microporosity levels was sufficient to shift the strut modulus below a threshold value resulting in a swing in the equilibrium of local bone cell activity towards a greater degree of stable bone apposition [56]. Moreover, strut microstructure was considered to offer the possibility for entrapment of growth factors both for endothelial as well as osteogenic system accelerating bone regeneration process [1].

### 3.4 In vivo testing

All animals tolerated the procedure well and survived throughout the length of the experiment. Upon explantation all constructs appeared encapsulated in dense fibrous tissue. There was no sign of an abscess or perforation of the skin, Fig. 8. Histological examinations shown in Fig. 9 revealed fibrovascular ingrowth from the periphery towards the core in variable degrees. The spaces of the canals were occupied by mature blood vessels. Variety in size implicated an advanced stage of differentiation into vessels of different orders organized in a hierarchy from afferent arteriole to precapillary arteriole, capillary, postcapillary venule draining into an efferent vein. The intersection

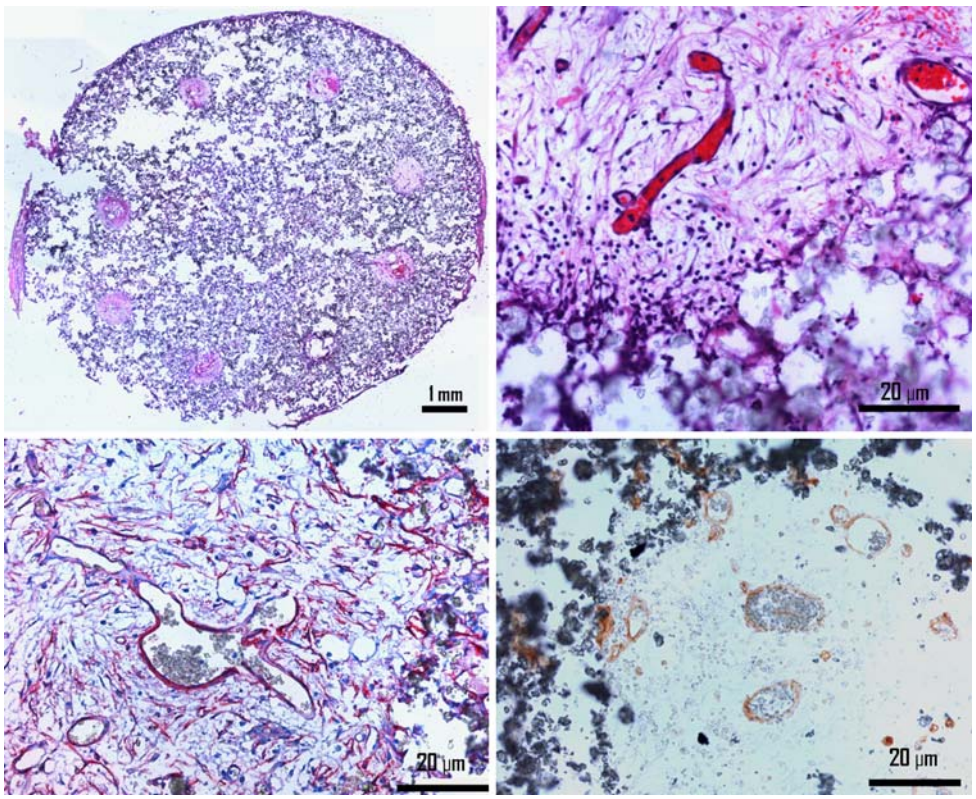


**Fig. 9** *Top left*: A planar view of the entire scaffold. The entire area of the matrix is covered with fibrovascular elements as demonstrated by a marked basophilic staining. The open canal spaces (CS) at the sites of the perforations demonstrate eosinophillic staining characteristic for apposition of extracellular matrix and red blood cells (thrombi) in the newly formed vessels. The remains of a fibrous capsule are seen at the periphery (FC) (Haemotoxylin–Eosin [HE] staining, merged image, 25×). *Top right*: Detailed view of the intersection between canal space and matrix. The neocapillaries (NC) are surrounded by loose fibrous tissue with scarce spindle like fibroblasts (FB) with dark blue (basophilic) nuclei and extracellular matrix staining pink (light eosinophillic). At the margins of the canal space there is a foreign body reaction characterized by granulocytic infiltration (GR), here seen as an accumulation of nuclei in this area. (HE, 200×). *Bottom left*: Detailed view of the intersection between canal space and matrix. The positive immunohistological staining for smooth muscle actin reveals a high degree of maturation after 4 weeks with colonization of the extramural site of the vessels with smooth muscle and pericytes.(Smooth muscle actin, Haematoxylin counterstaining, 200×) *Bottom right*: Immunohistology with lectin displays the presence of an endothelial lining of a functional vascular network. (Lectin, 200×)

between this newly formed fibrovascular tissue and the matrix displayed some degree of foreign body reaction with polymorphonuclear cells and fibrosis. The central areas in the canals were comprised of loose fibrovascular tissue. The matrix was invaded from host cells as demonstrated by multiple basophilic stained nuclei. However, there was no formation of an organized vascular network, such as in the canal spaces. To identify the phenotype of these cells, immunocytochemical staining with CD31, an endothelial cell specific marker, was performed. A multitude of the cells appeared positive for endothelial staining. In no histological views, however, could we confirm the presence of bone remodelling processes like bone formation or osteoclast activity. To identify the phenotype of these cells, immunocytochemical staining with lectin, an endothelial cell specific marker, was performed. The vascular network after 4 weeks had evolved into a mature neocapillary bed as displayed by alpha-smooth muscle actin immunocytochemical staining.

## 4 Conclusions

Bone graft scaffolds based on HA which contained different levels of porosity to promote vascularisation during bone regeneration process were prepared and investigated in vivo. Cylindrical shaped bone graft scaffolds which contained micropores (<1 μm in diameter, due to incomplete sintering), mesopores (1–100 μm in diameter, formed by inter-agglomerate pores) and macropores (>100 μm, created by printing to permit invasion of endothelial system) were formed by three dimensional printing of bimodal powder mixtures of coarse (50 μm) and fine grained (4 μm) HA powders. While rapid assimilation and long-term integrity are favoured by more porous structures, mechanical resilience during surgery and stability during the initial period of integration are favoured by more dense structure. Hence, optimisation of adequate porosity structure fulfilling both requirements is a challenge.

Foreign body reaction with accompanying fibrosis and granulocytic infiltration and neovascularization were comparable to biogenic matrices implanted subcutaneously in the same model [13]. Evolution of the neovascular network into a mature angial bed organized into vessels with different orders of hierarchy can be accomplished with gradual disintegration of the matrix. Further in vivo studies with bone specific growth factors termed bone morphogenetic proteins (BMP) might cause remodelling of the vascular and osseous elements within the matrix into a bone organoid with haversian units and myeloid areas.

## References


1. K. A. HING, *Int. J. Appl. Ceram. Technol.* **2** (2005) 184
2. A. A. WHITE, S. M. BEST and I. A. KINLOCH, *Int. J. Appl. Ceram. Technol.* **4** (2007) 1
3. J. R. JONES and L. L. HENCH, *Curr. Opin. Solid State Mater. Sci.* **71** (2003) 301
4. A. J. SALGADO, O. P. CAUTINHO and R. L. REIS, *Macromol. Biosci.* **4** (2004) 743
5. K. D. KARAGEORGIOU, *Biomaterials* **37** (2005) 533
6. C. D. HOLY, M. S. SHOICHET and J. E. DAVIES, *J. Biomed. Mater. Res.* **51** (2000) 376
7. R. Z. LEGEROS, *Clin. Orthop. Relat. Res.* **395** (2002) 81
8. S. DOROZHKIN, *J. Mater. Sci.* **42** (2007) 1061
9. U. KNESER, P. M. KAUFMANN, H. C. FIEGEL, J. M. POLLOK, D. KLUTH, H. HERBST and X. ROGIERS, *J. Biomed. Mater. Res.* **47** (1999) 494
10. A. D. BACH, J. P. BEIER, J. STERN-STAETER and R. E. HORCH, *J. Cell. Mol. Med.* **8** (2004) 413
11. K. NORRBY, *J. Cell. Mol. Med.* **10** (2006) 588
12. O. C. CASSELL, S. O. HOFER, W. A. MORRISON and K. R. KNIGHT, *Br. J. Plast. Surg.* **55** (2002) 603
13. E. POLYKANDRIOTIS, R. E. HORCH, A. ARKUDAS, A. LABANARIS, K. BRUNE, P. GREIL, A. D. BACH, J. KOPP, A. HESS and U. KNESER, *Adv. Exp. Med. Biol.* **585** (2006) 311
14. E. POLYKANDRIOTIS, J. TJIAWI, S. EULER, A. ARKUDASN, A. HESS, K. BRUNE, P. GREIL, A. LAMETSCHWANDTNER, R. E. HORCH and U. KNESER, *Microvasc. Res.* **1** (2008) 25
15. E. POLYKANDRIOTIS, A. ARKUDAS, S. EULER, J. P. BEIER, R. E. HORCH and U. KNESER, *Handchir. Mikrochir. Plast. Chir.* **38** (2006) 217
16. U. KNESER, E. POLYKANDRIOTIS, J. OHNHOLZ, K. HEIDNER, L. GRABINGER, S. EULER, K. AMANN, A. HESS, K. BRUNE, P. GREIL, M. STÜRZL and R. E. HORCH, *Tissue Eng.* **12** (2006) 1721
17. E. POLYKANDRIOTIS, R. E. HORCH, M. STURZL, U. KNESER, *J. Cell. Mol. Med.* **11** (2007) 6
18. P. DUCHEYNE, M. MARCOLONGO and E. SCHEPERS, "Bioceramic composites." In *An Introduction to Bioceramics*, edited by L. L. HENCH and J. WILSON (New York: World Scientific Publishing Co., 1993) p. 281
19. W. BONFIELD, "Design of bioactive ceramic-polymer composites." In *An Introduction to Bioceramics*, edited by L. L. HENCH and J. WILSON (New York: World Scientific Publishing Co., 1993) p. 299
20. G. DE WITH and A. J. CORBIJN, *J. Mater. Sci.* **24** (1989) 3411
21. J. LI, L. HERMANSSON and R. SOREMARK, *J. Mater. Sci. Mater. Med.* **4** (1993) 50
22. J. LI, B. FARTASH and L. HERMANSSON, *Biomaterials* **16** (1995) 417
23. J. D. SANTOS, P. L. SILVA, J. C. KNOWLES, S. TALAL and F. J. MONTEIRO, *J. Mater. Sci. Mater. Med.* **7** (1996) 187
24. K. KONDO, M. OKUYAMA, H. OGAWA and Y. ABE, *J. Am. Ceram. Soc.* **67** (1984) C 222
25. F. C. M. DRIESSENS, *J. Biosci.* **35** (1980) 357
26. J. R. JONES and L. L. HENCH, *Curr. Opin. Solid State Mater. Sci.* **71** (2003) 301
27. L. L. HENCH, *Biomaterials* **19** (1998) 1419
28. E. C. SHORS and R. E. HOLMES, "Porous hydroxyapatite." In *An Introduction to Bioceramics*, edited by L. L. HENCH and J. WILSON (New York: World Scientific Publishing Co., 1993) p. 181
29. S. PRAMANIK, A. K. AGARWAL, K. N. RAI and A. GARG, *Ceram. Int.* **33** (2007) 419
30. J. WERNER, B. LINNER-KRCMAR, W. FRIESS and P. GREIL, *Biomaterials* **23** (2003) 4285

31. M. FABBRI, G. C. CELOTTI and A. RAVAGLIOLI, *Biomaterials* **16** (1995) 225
32. P. SEPULVEDA, J. G. P. BINNER, S. O. ROGERO, O. Z. HIGA and J. C. BRESSIANI, *J. Biomed. Mater. Res.* **50** (2000) 27
33. D. M. ROY and S. K. LINNEHAN, *Nature* **247** (1974) 220
34. S. DEVILLE, E. SAIZ, K. R. NALLA and P. A. TOMSIA, *Science* **311** (2006) 515
35. C. X. F. LAM, X. M. MO, S. H. TEOH and D. W. HUTMACHER, *Mater. Sci. Eng. C* **20** (2002) 49
36. H. SEITZ, W. RIEDER, S. IRSEN, B. LEUKERS and C. TILLE, *J. Biomed. Mater. Res.* **B 74** (2005) 782
37. R. CHUMNANKLANG, T. PANYATHAMMAPORN, K. SITTHISERIPRATIP and J. SUWANPRATEEB, *Mater. Sci. Eng.* **C 27** (2007) 914
38. B. LEUKERS, H. GÜLKAN, S. H. IRSEN, S. MILZ, C. TILLE, M. SCHIECKER and H. SEITZ, *J. Mater. Sci.* **16** (2005) 1121
39. H. Y. SOHN and C. MORELAND, *Can. J. Chem. Eng.* **46** (1968) 162
40. A. R. DEXTER and D. W. TANNER, *Nature Phys. Sci.* **238** (1972) 31
41. P. A. CUNDALL and O. D. L. STRACK, *Geotechnique* **29** (1979) 47
42. G. T. NOLAN and P. E. KAVANAGH, *Powder Technol.* **72** (1992) 149
43. C. A. ANDERSSON, *J. Am. Ceram. Soc.* **79** (1996) 2181
44. J. A. FUNK and D. R. DINGER, *Predictive Process Control of Crowded Particulate Suspensions* (Norwell, Massachusetts: Kluwer Academic Publishers, 1994)
45. J. A. FUNK, D. R. DINGER, *Ceram. Bull.* **67** (1988) 890
46. R. Z. LEGEROS and J. P. LEGEROS, "Dense hydroxyapatite." In *An Introduction to Bioceramics*, edited by L. L. HENCH and J. WILSON (New York: World Scientific Publishing Co., 1993) p. 154
47. M. BOHNER, *Int. J. Care. Inj.* **31** (2000) 37
48. L. L. HENCH, *J. Am. Ceram. Soc.* **74** (1991) 1487
49. K. A. HING, S. M. BEST and W. BONFIELD, *J. Mater. Sci. Mater. Med.* **10** (1999) 134
50. R. W. RICE and W. R. GRACE, *J. Mater. Sci.* **31** (1996) 102
51. C. A. ANDERSSON, *J. Am. Ceram. Soc.* **79** (1996) 2181
52. K. DE GROOT, "Ceramics of calcium phosphate, preparation and properties." In *Bioceramics of Calcium Phosphate*, edited by K. DE GROOT (Boca Raton, FL: CRC-Press, 1983) p. 102
53. T. D. TONYAN and L. J. GIBSON, *J. Mater. Sci.* **27** (1992) 6371
54. L. J. GIBSON and M. F. ASHBY, *Cellular Solids, Structure and Properties*, 2nd edn. (Oxford: Pergamon Press, 2001)
55. R. E. HOLMES, *Plast. Reconstr. Surg.* **63** (1979) 626
56. A. BIGNON, J. CHOUTEAU, J. CHEVALIER, G. FANTOZZI, J. P. CARRET, P. CHAVASSIEUX, G. BOIVIN, M. MELIN and D. HARTMANN, *J. Mater. Sci. Mater. Med.* **14** (2003) 1089